The Nature of Oxygen Vacancy and Spinel Phase Integration on Both Anionic and Cationic Redox in Li-rich Cathode Material

Qingyuan Li[a], De Ning[b], Dong Zhou[b], Ke An[c], Deniz Wong[b], Lijuan Zhang[d], Zhenhua Chen[d], Götz Schuck[b], Christian Schulz[b], Zijian Xu[d], Gerhard Schumacher[b] and Xiangfeng Liu[a*]

[a] Center of Materials Science and Optoelectronics Engineering, College of Materials Science and Optoelectronic Technology, University of Chinese Academy of Sciences, Beijing 100049, P. R. China.

[b] Helmholtz-Center Berlin for Materials and Energy, Hahn-Meitner-Platz 1, D-14109 Berlin, Germany.

[c] Neutron Scattering Division, Oak Ridge National Laboratory, Oak Ridge, Tennessee, 37830, USA.

[d] Shanghai Synchrotron Radiation Facility, Shanghai Institute of Applied Physics, Chinese Academy of Sciences, Shanghai 201204, P. R. China.

*E-mail: liuxf@ucas.ac.cn

Abstract

Tuning the anionic redox chemistry ($O^{2-} \rightarrow O_2^{n-}$) activity and reversibility by the crystal and/or electronic modulation is essential for Li-rich oxides cathode materials. Herein, we report a facile strategy to improve the activity and reversibility of both anionic and cationic redox by integrating oxygen vacancies and spinel phase. The initial specific capacity (216.1 mAh g^{-1} v.s 316.3 mAh g^{-1}), Coulomb efficiency (80% v.s 94.8%), long-term cycling stability (1000 cycles at 5C) and voltage decay have all been greatly improved due to the largely suppressed irreversible oxygen release. The underlying modulation mechanism has been unraveled. Firstly, the introduction of oxygen vacancies decreases the covalency of TM-O and the density of the state of O 2p band, which mitigates the irreversible oxygen release during oxygen redox. Secondly, the spinel phase integration induced by oxygen vacancies not only improves the Li-ion conductivity and the rate capability due to its 3D Li^+ channel and the expanded Li layer but also enhances the structure stability. Thirdly, the first-principle calculations indicate that the increase of delocalized electrons around transition metal also intensifies the MnO_6 octahedral distortion and the inactive Mn-ions are partially activated during the first cycle and participate in the charge compensation. This study sheds some new light into designing the high-performance Li-rich layered oxide cathode materials by regulating the anionic and cationic redox with the incorporation of oxygen vacancies and spinel phase.

Keywords: lithium-ion battery; Li-rich cathode; anionic redox; neutron diffraction; X-ray absorption spectra

1. Introduction

With the development of electric vehicles, cathode materials with high energy density and high safety are urgently demanded.[1-4] For the next generation battery, Li-rich Mn-based (LRM) cathode materials are deemed the most promising candidate due to their high capacity (>300 $mAhg^{-1}$),[3, 5-9] originating from the redox couples of both transition metal cations and oxygen anion. This has been verified by some pioneering researches.[10-15] Especially, the reversible anionic redox processes (O_2^- / O_2^{n-}, where n = 1, 2 or 3) have been verified with transmission electron microscopy (TEM) and neutron powder diffraction (NPD) by Tarascon.[16, 17] Additionally, Ceder et al. have revealed the transition metal Mn plays an important role in improving the electrochemical performances when it participates in charge compensation.[5, 18, 19] Although LRM cathode materials have high specific capacity, the practical application has been seriously hindered by the average voltage attenuation, sluggish Li^+ migration kinetics and poor cyclic performance.[20, 21] Recently, Yu et al. have illustrated that the voltage fade is closely related to the irreversible oxygen release and the reduction of transition metal.[22] And Bruce et al. have shown the voltage hysteresis can be avoided by introduction of superstructure.[23] Our group has also proposed an integrated strategy that combines the advantages of Li_2SnO_3 coating, Sn^{4+} doping and the induced-spinel structure to tune the activity and reversibility of LRM cathode materials.[24] Therefore, it is highly desirable to explore some effective strategies to improve the anionic redox and suppress the irreversible O_2 release.

Oxygen vacancy engineering has aroused much interest as an effective strategy to tune the electronic structure and enhance the activity of some electrocatalysts.[25, 26] In addition, the positive roles of oxygen vacancies have also been verified in the transition metal oxides as energy storage materials.[27-29] Dunn et al. have illustrated the electron/ion conductivity, and the electrochemical performance of transition metal oxides can be intrinsically improved by incorporating oxygen vacancies.[30] Liu et al. have verified that the surface oxygen vacancies can reduce the oxygen release and enhance Li^+ diffusion in Li^+ batteries.[27] However, the nature of the introduction of oxygen vacancies on the anionic and cationic redox chemistry is still not very clear.

Herein, we synthesize the cobalt-free Li-rich Mn-based oxides cathode materials with the incorporation of surface oxygen vacancies and spinel phase by a facile reduction method. The underlying mechanism of the integration of oxygen vacancy and spinel phase on the activity and reversibility of both anionic and cationic redox has been unraveled by means of neutron diffraction, (*in situ)* X-ray diffraction (XRD), spherical aberration corrected microscopy, X-ray absorption spectroscopy (XAS), differential electrochemical mass spectrometry (DEMS), first-principle calculations, *ex situ* X-ray photon spectroscopy (XPS) and resonant inelastic X-ray scattering (RIXS).

2. Experimental Section

Synthesis: Our previous method for the synthesis of precursor $Ni_{0.25}Mn_{0.75}CO_3$ is employed in this experiment.[24] In order to synthesize $Li_{1.2}Mn_{0.6}Ni_{0.2}O_2$, the precursor

and the $LiOH{\cdot}H_2O$ (5 % excess) are mixed by stoichiometric amounts, and carefully grinded, then the mixture is calcined at a temperature of 900 °C for 12 h with a heating rate of 5 °C min^{-1}. To obtain the aimed oxygen vacancy (OV) material, the obtained product of powder-like $Li_{1.2}Mn_{0.6}Ni_{0.2}O_2$ is then mixed with the ammonium bicarbonate (NH_4HCO_3) by the molar ratio of 3:1 in the tube furnace filled with argon. Then the product is carefully grinded, and the mixture is calcined at a lower temperature of 600 °C for 10 h with a heating rate of 1 °C min^{-1} under argon atmosphere.

Material Characterization: XRD is employed to investigate the crystal structure of the samples in the 2θ range of 10–80° on Smartlab (Rigaku, Cu K_α), using a step size of 0.02° and a scan rate of 10° per minute. The element content has been tested by inductively coupled plasma mass spectrometry (ICP-MS, Agilent 7700). The structures and morphologies of the samples are further investigated by using transmission electron microscopy (TEM, Philips, Tecnai G2 F30). In order to characterize the detailed information of the structures in atomic scale, aberration-corrected scanning transmission electron microscopy (SEM, JEM ARM200F JEOL, Tokyo, Japan) is used, assisted by two CEOS (CEOS, Heidelberg, Germany) probe aberration correctors. The elements state of the samples is investigated with an AXIS Supra by Kratos Analytical Inc. using monochromatized Al Kα radiation (hv = 1486.6 eV, 300 W) and Ag Lα (hv = 2984.4 eV, 450 W) as X-ray source with a base pressure of 10^{-9} torr and Thermo Escalab 250Xi. The soft X-ray absorption spectroscopy (SXAS) of powder materials is carried out at the Russian–German Beamline of the synchrotron Bessy II at Helmholtz-

Zentrum Berlin (HZB), Germany. Data were collected in fluorescence yield (FY) mode at 25 °C under the vacuum of 10^{-9} Torr. SXAS of *ex-situ* batteries is conducted in total electron yield (TEY) mode at 4B7B beamline of the Beijing Synchrotron Radiation Facility (BSRF), the results were normalized to the incident photon flux I_0 measured by a fresh gold target and FY modes at beamline BL08U1-A with the vacuum of 10^{-5} - 10^{-6} Torr at the Shanghai Synchrotron Radiation Facility (SSRF). The hard XAS is performed at the beamline 1W1B at BSRF and the beamline KMC2 at HZB. The soft resonance inelastic X-ray scattering (RIXS) is performed at the PEAXIS beamline of HZB. DEMS is measured in an i-DEMS 100 instrument (Linglu) with an EI-70 eV ion source and SEM-100 V detector, and the operando DEMS cells are conducted at a current density of 0.075C between 2.0 and 4.8 V using battery tester (LAND CT2001A).

Electrochemical Measurements: Electrodes are composed of active materials (80 wt%), carbon black (10 wt%), and polyvinylidene fluoride (10 wt%), mixing in N-methyl pyrrolidinone to form a mud-like mixture, then spread it evenly on aluminum foil, dried in vacuum for 12 h at the temperature of 120°C. The mass of the active materials loaded on each electrode was approximately 2 mg. The potentiostatic intermittent titration technique (PITT) and the electrochemical impedance spectroscopy (EIS) are tested on an electrochemical workstation (Metrohm-Autolab, PGSTAT 302N), which keeps an amplitude of 5 mV and a frequency range from 100 kHz to 0.1

Hz. The battery tester (NEWARE) was used to test the Galvanostatic charge–discharge cycling at various current densities.

Neutron powder diffraction (NPD): The data are obtained on the VULCAN beamline at the Spallation Neutron Sources (SNS) in the Oak Ridge National Laboratory,[31, 32] the incident beam has the size of 5 mm×12 mm, and 5 mm receiving collimators, the bandwidth of the incident beam was 0.7-3.5 Å, and it was selected by employing the double-disk choppers at a speed of 30 Hz, 0.5−2.5 Å d-space was allowed in the diffracted patterns in the $\theta \pm 90°$ detector banks. The $\Delta d/d$ is around 0.25 % at the high-resolution mode. The power of SNS was at nominal 1,400kW，and the NPD data collection takes up to three hours at the temperature of 25 ℃，the VDRIVE software was used to reduce the data. Full-pattern Rietveld refinement was carried out using the GSAS programs with the EXPGUI interface.[33]

Computation method: First-principle calculations were performed by the density functional theory (DFT) using the Vienna Ab-initio Simulation Package (VASP).[34] The generalized gradient approximation (GGA) with the Perdew-Burke-Ernzerhof (PBE) functional were used to describe the electronic exchange and correlation effects.[35-37] Uniform G-centered k-points meshes with a resolution of $2\pi * 0.03$ Å^{-1} and Methfessel-Paxton electronic smearing were adopted for the integration in the Brillouin zone for geometric optimization. The simulation was run with a cutoff energy of 500 eV throughout the computations. These settings ensure convergence of the total energies

to within 1 meV per atom. Structure relaxation proceeded until all forces on atoms were less than 1 meV $Å^{-1}$ and the total stress tensor was within 0.01 GPa of the target value.

We used the hexagonal structure of $Li_3Mn_3O_6$ (space group: $R\bar{3}m$) as initial structure to build the $Li_{1.2}Mn_{0.6}Ni_{0.2}O_{2-X}$ compound. Firstly, we convert the hexagonal structure of $Li_3Mn_3O_6$ into its rhombohedral representation, thus the chemical formula of $Li_3Mn_3O_6$ becomes $Li_1Mn_1O_2$. Secondly, we built a $5 \times 1 \times 1$ supercell of $Li_1Mn_1O_2$ along the x-axis direction, thus we get the $Li_5Mn_5O_{10}$ structure. Thirdly, one Mn atom is replaced by Li, while another Mn atom is replaced by Ni atom, thus the $Li_6Mn_3Ni_1O_{10}$ structure, i.e. $Li_{1.2}Mn_{0.6}Ni_{0.2}O_2$ is produced. For the O vacancy containing structure, we randomly delete one O atom. Finally, we have done fully geometry optimization, i.e., the lattice parameters (a, b, c, α, β, γ) and atomic positions.

3. Results and Discussion

3.1 Structure Analysis

The true elemental content of pristine ($Li_{1.2}Mn_{0.6}Ni_{0.2}O_2$) and oxygen-vacancy (OV, $Li_{1.2}Mn_{0.6}Ni_{0.2}O_{2-\delta}$) samples has been determined by ICP-MS, and the results of both materials are approximately the same as shown in the Table S1. The refined powder X-ray diffraction (XRD) patterns of both samples are shown in Fig. S1†. All diffraction peaks of both samples can be indexed by rhombohedral structure with a space group of $R\bar{3}m$. In addition, a small amount of spinel phase with a space group of $Fd\bar{3}m$ can be detected in OV samples as shown in Fig. S1b.† In order to clarify the

existence of oxygen vacancies in the OV sample, Rietveld refinements of NPD patterns have been performed thanks to its sensitivity to the oxygen vacancies. Fig. 1 shows the refined results of NPD patterns with the two mentioned crystal structures. As it shows, the oxygen occupancies of the OV sample are reduced to 96.7% from 100% of the pristine sample and the spinel content accounts for approximately 4%, indicating that both oxygen vacancies and spinel phase have been incorporated successfully. The refined structure parameters for each sample are listed in Table 1, and the detailed site occupancies of both samples are summarized in Table S2†. As shown in Table 1, the parameters of the OV sample are increased compared with the pristine material, which is caused by the reduction expansion, and it comes from two competitive aspects: (1) the increase in cation radii is accompanied by reduction of transition metal ions valence which leads to the I_{LiO2} expansion. (2) The lattice contraction is accompanied by the formation of vacancies due to the electrostatic interactions. Generally, the increase of cation radius is more dominant than the small anion extraction in nonstoichiometric compounds.[18, 38] The crystal structure image is shown in Fig. 1c and d based on the refined structure parameters of NPD. It is worth noting that I_{LiO2} of the OV sample is wider than that of the pristine sample, which may be caused by the spinel phase and reduction expansion. Moreover, the structure of the OV sample is more stable than that of the pristine material, which can be verified by the reduced S_{MO2} layer spacing in the OV sample[39] due to the decreased covalence of the TM-O bond.[24, 40, 41] In the Table S2, the Li/Ni mixing is slightly increased, which is beneficial to the suppressing of the

structural phase change and voltage maintain due to preventing the manganese from falling into the intermediary tetrahedral sites.

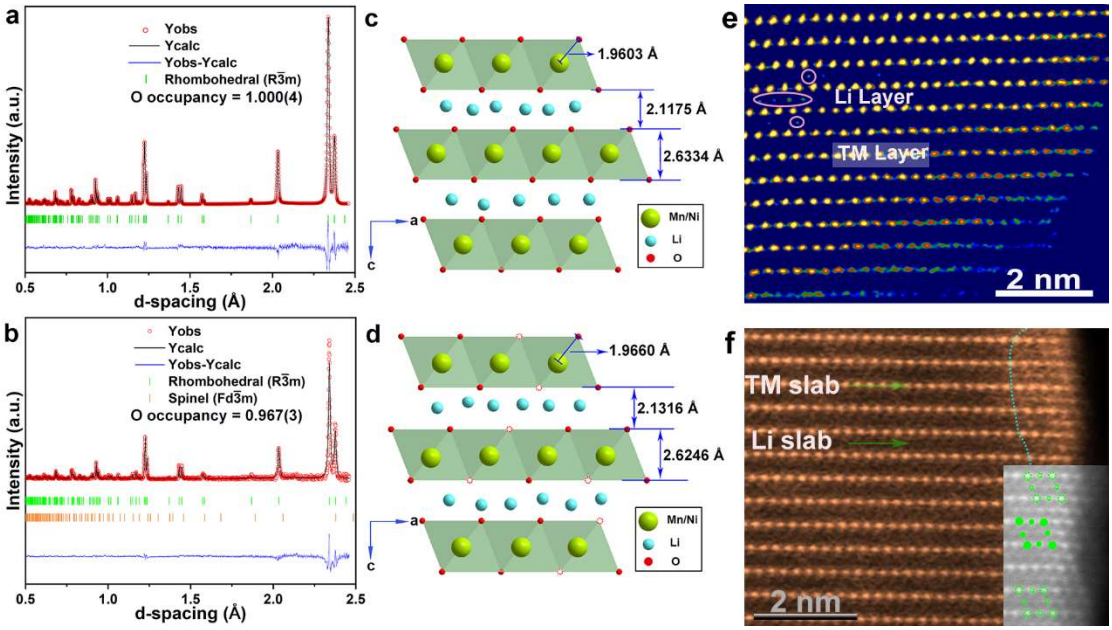

Fig. 1 (a and b) Powder TOF ND refinement patterns of the pristine and OV samples, respectively. The oxygen vacancy of the OV sample increase by 3.3% compared to the pristine material. (c and d) The crystal models and corresponding cell parameters. The corresponding labeled parameters are calculated by the formula: $I_{(LiO2)} = (c/3) - S_{(MO2)}$); ($S_{(MO2)} = 2[(1/3) - z_{ox}]c$, and the values of c and z_{ox} are from the refinement results of powder TOF ND in the (a) and (b), respectively. (e and f) HAADF-STEM images of pristine and OV sample along the $[1\bar{1}0]$ direction, respectively. The ellipse circles represent the mixing of Li/Ni. For comparison, the spinel phase only in the OV sample.

The morphology of both samples is characterized by field emission scanning electron microscopy (FESEM) and transmission electron microscopy (TEM) with energy-dispersive X-ray (EDX) elements mapping as Fig. S2† shown. From the figures, we can find that both samples are assembled into a sphere shape (~3 um) by primary particles without clear difference. In order to further intuitively illustrate the difference and the existence of the spinel phase in the OV sample, aberration corrected scanning transmission electron microscopy (AC-STEM) in the high-angle annular dark-field

(HAADF) mode has been used as shown in Fig 1e and f. The bright spots represent Ni and Mn, which have higher atomic numbers. As a comparison, the light atoms O and Li are shown by dark spots. In Fig. 1e, we can only find one type of atomic arrangement along the $\mathbf{[1\bar{1}0]}$ direction, which can be classified as the layered structure ($R\bar{3}m$). Moreover, the ellipse circles represent the Li/Ni mixing. The spinel structure, however, can be only indexed on the surface as shown in Fig. 1f. The dashed line shows the boundary between the layered structure and the spinel phase, and the inset shows the magnified spinel area and the crystal model with $Fd\bar{3}m$ space group. The results of both NPD and AC-STEM evidence that the oxygen vacancies and the spinel phase have been successfully introduced in the OV sample.

Table 1 The structure parameters derived from Rietveld refinement of NPD

Sample	a (Å)	c (Å)	V (Å^3)	Z_{ox}	$S_{(MO2)}$ (Å)	$I_{(LiO2)}$ (Å)	TM-O (Å)	R_p (%)
Pristine	2.8573(4)	14.2527(3)	100.77(3)	0.24095	2.6334	2.1175	1.9603(4)	4.51
OV	2.8613(4)	14.2686(4)	101.17(3)	0.24136	2.6246	2.1316	1.9660(4)	4.71

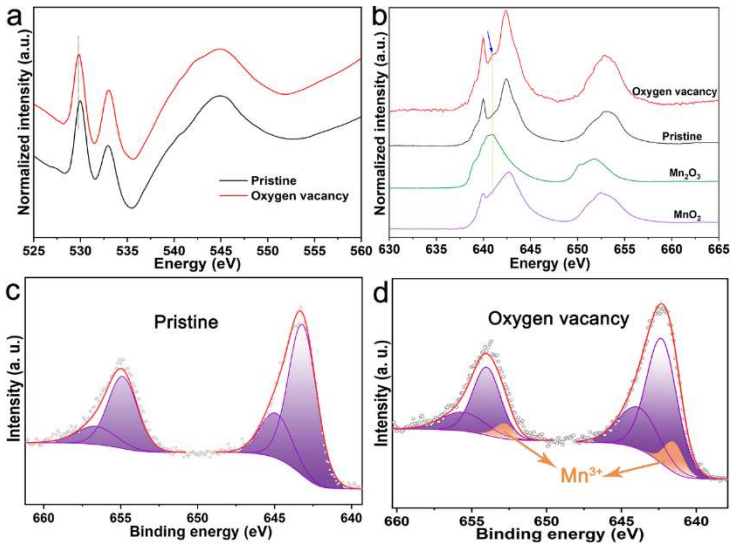

Fig. 2 (a) O K-edge of soft XAS of pristine and OV sample with TEY mode, respectively. The peaks shift to low energy means oxygen vacancy has been introduced.

(b) Mn L-edge of soft XAS of pristine, OV sample, MnO_2 and Mn_2O_3 in OCV state with TEY mode, respectively. The blue arrow shows the existence of Mn^{3+} in the OV sample. (c) XPS of pristine sample for Mn 2p. (d) XPS of OV material, as a comparison, there is Mn^{3+} in the OV material indicating the existence of spinel phase.

To further explore the preferred location of oxygen vacancies, SXAS and XPS have been performed as shown in Fig. 2. Fig. 2a shows the O K-edge of both samples in TEY mode. We can clearly find the pre-edge peak of the OV sample shifts to lower energy with obviously decreased intensity compared to that of the pristine one, which can be ascribed to the change of local electronic structure of O atoms and the reduction of TM-O covalence when oxygen vacancies are introduced in the surface.[27, 40, 42] As a comparison, the O K-edge spectra from the bulk of both samples collected in FY mode in Fig. S3, † which has a probing depth of 100-200 nm, are almost the same, indicating the oxygen vacancies only exist on the surface of materials. In addition, the XPS spectra of O 1s have been shown in Fig. S4.† We can observe that the main peak of the OV sample shows lower intensity and it located at lower binding energy compared to that of the pristine one manifesting the formation of oxygen vacancies on the surface of the powder particles.[27] To further study the spinel phase, Mn L-edge absorption spectra have been collected in TEY mode as shown in Fig. 2b. Firstly, both samples are substantially unchanged in the peaks of L_2 and L_3. However, a new peak appears at approximately 641 eV as shown by the blue arrow which means manganese 3d bands shift to higher occupancies due to the reduction of Mn^{4+} to Mn^{3+}.[43-45] Moreover, to confirm the effect of Mn^{3+} more intuitively, the curves of Mn^{4+} (MnO_2) and Mn^{3+} (Mn_2O_3) are shown in Fig. 2b. Clearly, a similar feature between the new peak of the

OV sample and that of Mn_2O_3 can be seen at the dashed line.[46] The slightly lower valence Mn means it can be oxidized to Mn^{4+} to participate in the charge compensation. As a comparison, the Mn L-edge spectra also have been conducted with FY mode as shown in Fig. S5.† No clear differences can be seen for both samples, suggesting the valence of Mn in the bulk phase is unchanged. This is a result of the near-surface location of the oxygen vacancies and spinel phase.

To further analyze the Mn^{3+} and eliminate the effect of Ni LMM auger peaks (Fig. S6†), the XPS spectra of Mn 2p have been tested with an Ag target as shown in Fig. 2c and d. The binding energy located at approximately 642.6, 644.4, 654.3 and 656.0 eV can be indexed as Mn^{4+} as shown in the purple areas, whereas Mn^{3+} can only be clarified at 641.5 and 652.8 eV in the oxygen vacancies sample as orange shadow region shows, and coupled with the slightly wider peaks due to the lower binding energy of Mn^{3+} as shown in the Fig. S6c.† This indicates the formation of oxygen-defects and spinel phase. To further confirm the Mn valence, Mn 3s spectra are tested in Fig. S7.† As shown in Fig. S7a† for comparison, the slightly widened peaks of Mn 3s in the OV sample also means that there may be Mn^{3+} because the Mn 3s width of Mn^{3+} is wider than that of Mn^{4+}. Fig. S7b† shows the splitting energy of Mn 3s of OV sample (4.61 eV) is wider than 4.42 eV of pristine material. According to the linear equation due to the relation between splitting energy of Mn 3s (ΔE_{3s}) level and Mn valence (υ_{Mn})[47]:

$$\upsilon_{Mn} = 9.67\text{-}1.27\ \Delta E_{3s}/eV.$$

The Mn valence of OV material is +3.82, indicating the existence of spinel $LiMn_2O_4$ in the rhombohedral structure, and the Jahn-Teller effect cannot occur because it requires manganese valence to be less than 3.5+.[48] Moreover, the existence of $LiMn_2O_4$ may be proved by the Raman spectrum due to the characteristic peak at approximately 625 cm^{-1} and the charge-discharge curves at approximately 4.75 V in Fig. S8.†[6, 24, 49, 50] Therefore, the formation of oxygen vacancies and spinel phase on the surface have been successfully verified by the XRD, neutron powder diffraction, soft XAS and XPS.

3.2 Electrochemical Performances and Mechanisms

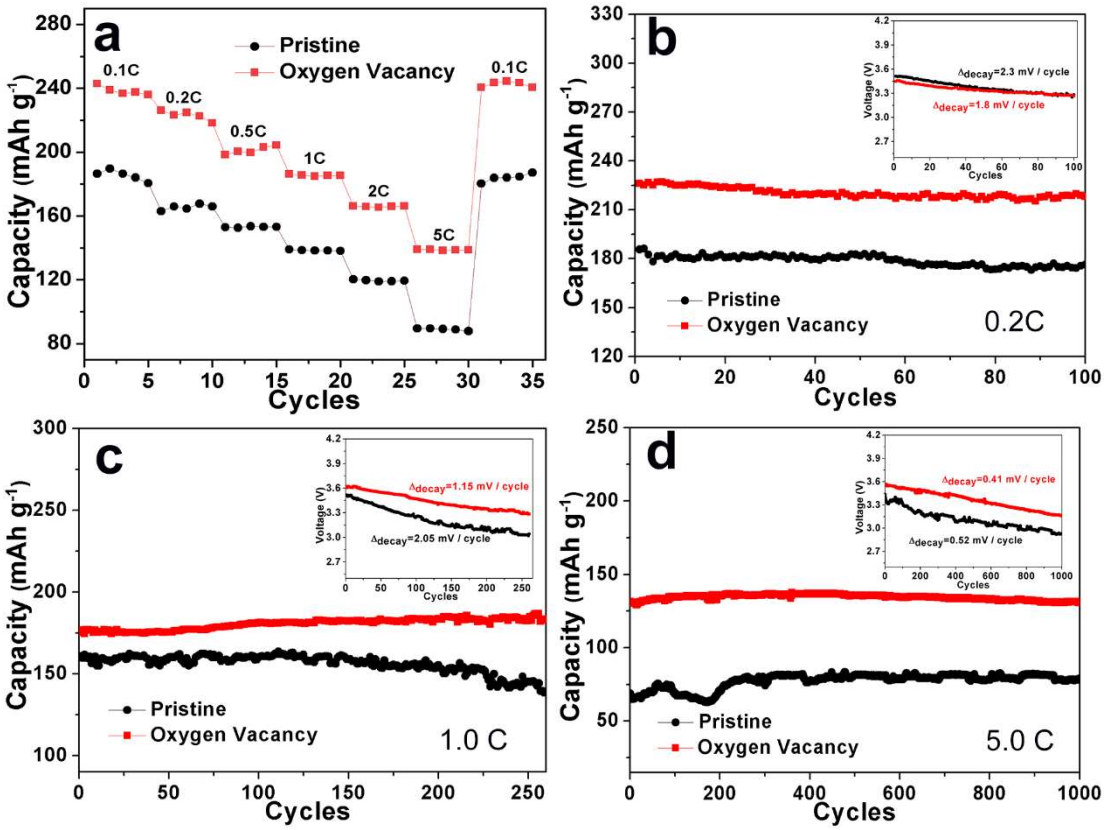

Fig. 3 The electrochemical performances of pristine and OV samples, respectively. (a) The rate capacity. (b-d) The cyclic performance at 0.2 C, 1.0 C and 5.0 C, respectively. The three insets show the voltage fading curves.

Fig. 3 shows the electrochemical performances of cathodes in Li-rich Li cells. The rate capacity from 0.1C to 5C (1C =250 mA g^{-1}) between 2 and 4.8 V was conducted as shown in Fig. 3a. We can find that the rate performance of the OV sample is substantially superior to that of the pristine material. Especially, the specific capacity of the OV sample is improved by approximately 55% compared to that of the pristine material at 5C rate. The outstanding rate performance can be attributed to the improved electron and Li^+ conductivity due to the increase of I_{LiO2} for this material with oxygen vacancies and spinel phase.[27, 30] To verify the Li^+ conductivity of the OV sample is better than that of the pristine, the PITT and the CV of various scan rates have been used to test the Li^+ diffusion coefficient as shown in the Fig. S9† and Fig. S10.† The diffusion coefficient (D) can be calculated by the following equation,[24] in which, the I and t stand for the titration current and time in each step, respectively, and the L represents the diffusion length.

$$D_{Li} = -[d \ln (I) / dt] \bullet [4L^2 / \pi^2]$$

The D_{Li} of pristine and OV samples are 9.68×10^{-14} and 1.20×10^{-13} cm^2 s^{-1}, respectively, during the discharge process, which is in line with the results of CV, 2.53×10^{-14} cm^2 s^{-1} and 4.93×10^{-14} cm^2 s^{-1} for pristine and OV samples, respectively, during the reduction process, based on the Randless-Sevcik equation as shown in Fig. S10†. The results show the OV sample has an excellent Li^+ conductivity because of the 3D Li^+ tunnel of spinel phase and the enlarged Li-ion diffusion layer, and these are consistent with the electrochemical performance.

In addition, Fig. S11† shows the Coulomb efficiency in the first cycle is 80% and 94.8% for pristine and OV samples, respectively. If we consider the theoretical capacity of this composite material can be calculated by the sum of LRM and spinel we would expect the theoretical capacity is approximately 230 mAh g^{-1}. However, the initial discharge capacity of pristine and OV samples is 216.1 mAh g^{-1} and 316.3 mAh g^{-1}, respectively, which significantly exceeds the theoretical capacity. This indicates that the capacity is derived not only from the transition metal Ni but also from some additional redox reactions, i.e. the anionic redox and the Mn redox which can be confirmed by the discharge curve at ~2.6 V due to the spinel phase.[24, 51, 52] This reduced Mn has been demonstrated in Fig. S12.† We can clearly find the Mn K-edge of OV sample shifts to the lower energy compared with the curves of pristine material and MnO_2, which means the valence state of Mn ion is less than +4 but greater than +3.5 of the occurrence of the Jahn-Teller effect. So, the high initial capacity of the OV sample originates from the enhanced anionic and cationic redox.

Fig. 3b-d show the cyclic stability at different current density. The cyclic stability of the OV sample is obviously enhanced regardless of the rate at 0.2 C, 1.0 C and 5.0 C. We can find the initial cyclic capacity is 216, 175 and 131 mAh g^{-1} at the current density of 0.2 C, 1 C and 5 C for OV sample, respectively. After 100 cycles, the discharge capacity of OV sample is 219 mAh g^{-1} with a capacity retention ratio of 97%. It is worth noting that the capacity of the OV sample is promoted approximately 4.6% to 183 mAh g^{-1} after 250 cycles at 1.0 C, and the capacity retention rate is about 100%

after 1000 cycles at 5C due to the stable structure. In comparison, for the pristine, the first discharge capacity is 186, 161 and 70 mAh g^{-1} at the current density of 0.2 C, 1 C and 5 C, respectively. The capacity retention rate is 94.6%, 85.7% and 110% at the corresponding current density. The increased capacity can be ascribed to the more thorough activation. The excellent performances have been compared in the Table S3†.

Voltage fading is a critical problem for LRM. However, the voltage decay is also suppressed by the introduced oxygen vacancies, which can produce less oxygen and decrease the lattice stress as shown in the insets of Fig. 3b-d. The voltage fading is 2.3, 1.15 and 0.41 mV/cycle at 0.2C, 1C and 5C for the OV, respectively, which is less than that of pristine (1.8, 2.05 and 0.52 mV/cycle at 0.2C, 1C and 5C). Moreover, the voltage profiles of different cycles have been shown in Fig. S13,† which shows the voltage decay has been significantly suppressed whether in rate capacity or various cyclic current density. The dQ/dV curves of both samples at different cycles are shown in Fig. S14.† The oxidation-reduction peaks at ~3.25 and ~3.8 V can be ascribed to the $Mn^{3+/4+}$ and $Ni^{2+/4+}$ redox couples, respectively.[53] The pristine sample shows a sluggish reaction kinetics until 25th cycle compared to the OV material at the highest cathodic peaks. Moreover, the peaks and shape of the OV sample are more obvious and stable than those of the pristine material even at the 101st cycle, which means the cations of OV sample are involved in the charge compensation and the structural damage is much less than in the pristine material.

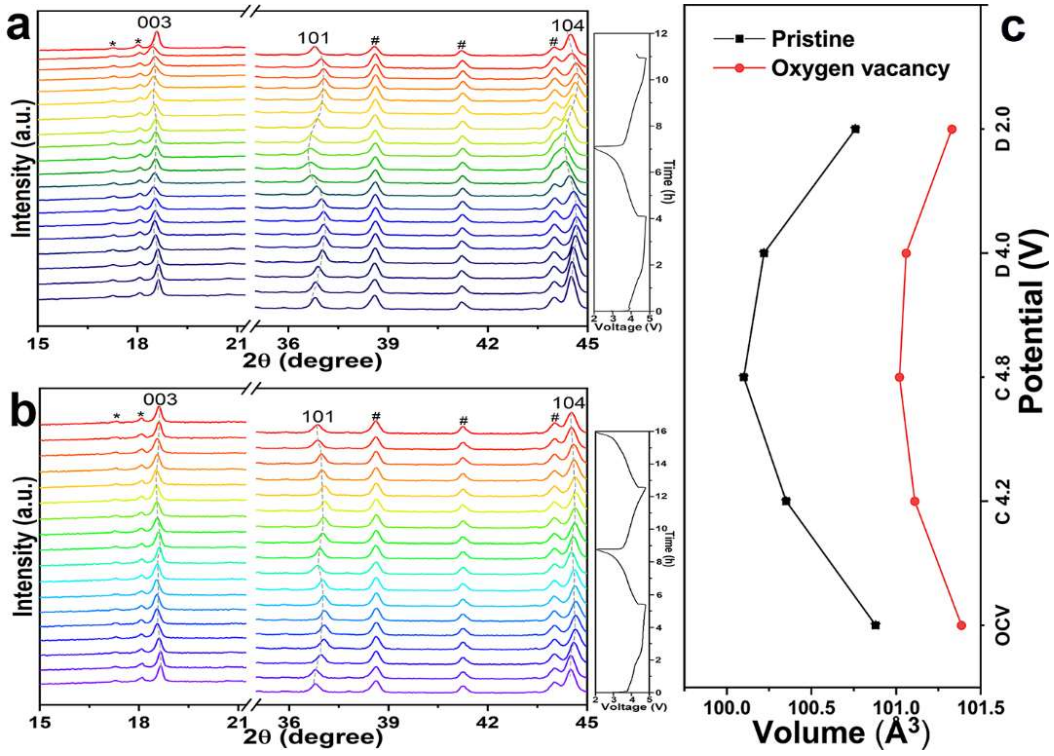

Fig. 4 In situ XRD patterns of (a) pristine and (b) OV sample during the first two cycles. The * and # represent Be and BeO from the cell window, the slight shift peaks of (003), (101) and (104) show a more stable structure of OV sample. (c) Cell volume change of pristine and OV samples at different charge-discharge states.

Fig. 4 shows the *in situ* XRD spectra in the first two cycles, illustrating the real-time structure evolution during the electrochemical reactions. At first, the unchanged peaks indexed with * and # can be attributed to Be and BeO, respectively, of the cell window. Except that, there are three characteristic peaks below 45° angle region, which can be assigned to (003), (101) and (104) with the $R\bar{3}m$ space group. It is worth noting that the change of these peaks of the pristine sample is more dramatical than that of OV material, which indicates there is a more stable framework in the OV sample. Further analysis indicates that the (003) peak shifts to lower 2θ angle but the (101) and (104) peaks move toward to the higher angles during the charge process, meaning the increased layer spacing (I_{LiO2}) of Li layers is caused by the enhanced electrostatic

repulsion between the adjacent oxygen layer with Li extraction from the Li layers.[54, 55] Conversely, the peaks shift to the opposite direction in the full discharge station compared with charge process, indicating the decrease of cell unit c-parameter and the contraction of I_{LiO2} due to the reduced repulsion caused by the inserted Li ion. Moreover, *ex situ* XRD has been used to investigate the lattice volume change at different charge and discharge states as shown in Fig. 4c. The cell volume evolution of the OV sample is smaller than pristine material, which indicates OV is more stable.

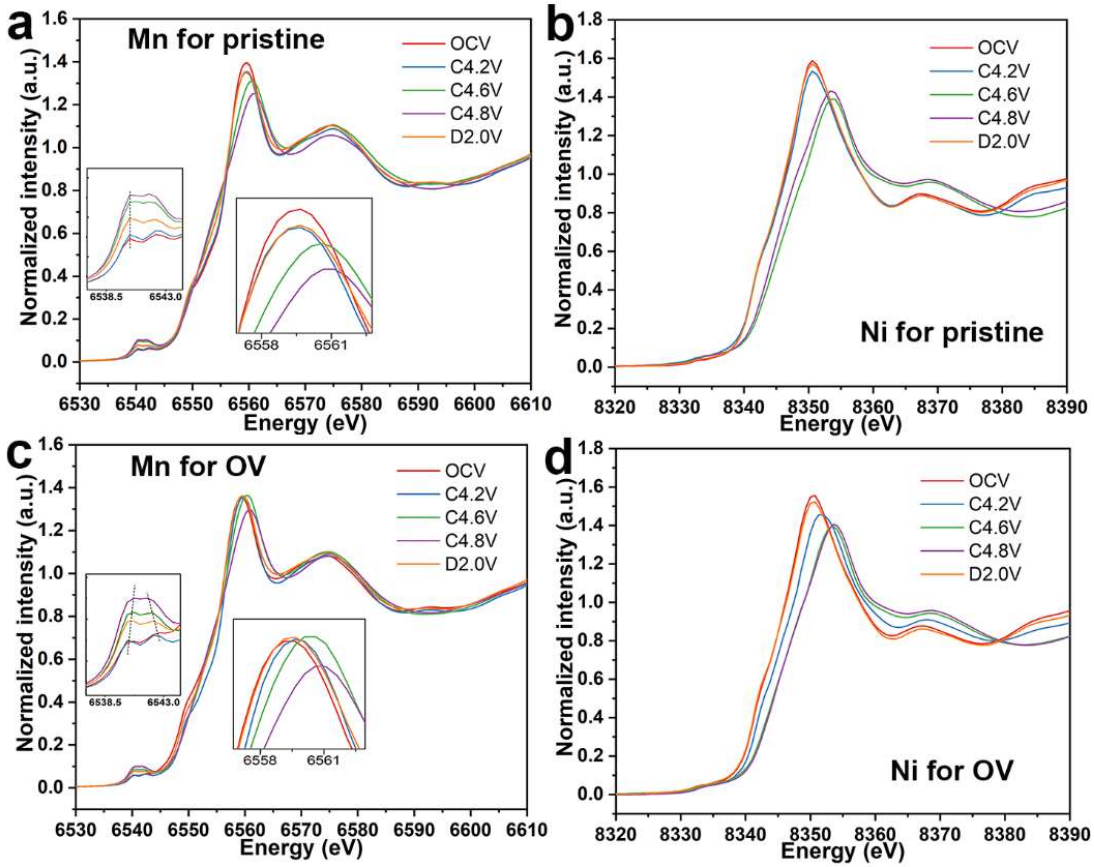

Fig. 5 *Ex situ* hard XAS of pristine and OV materials at the first cycle. Mn K-edge XANES of (a) pristine sample and (c) OV sample; Ni K-edge XANES of (b) pristine sample and (d) OV sample. The OCV, C and D represent open circuit voltage, charge and discharge, respectively.

Electrochemical performances are not only closely related to the crystal structure but also to the electronic structure. In order to demonstrate the electronic structure changes of the materials, *ex situ* hard X-ray absorption near-edge structure (XANES) spectra have been measured to test the K-edge information of transition metals at different charge-discharge states as shown in Fig. 5. The pre-edge peak of Mn K-edge is sensitive to the change of valence of Mn. According to the inset of Fig. 5a, the pre-peaks of Mn do not shift obviously in the pristine material during the first cycle. However, these OV samples have a weak change, which indicates Mn ion occurs minor oxidation in the OV sample, illustrating cation Mn ions participate in the charge compensation due to the spinel phase, and this is consistent with the previous discussions of XPS results. In addition to the position of the peaks indicating the valence state change, the intensity of pre-peaks describes the distortion of the octahedral structure. The intensity of pre-peaks first increases to the maximum and then decreases during the first charge-discharge process, which means the stability of the structure.[56] As shown in Fig. 5, the highest peaks are called “white line”, whose intensity and position are related to the occupancy of p states of TM atoms.[57] The white lines of Mn of pristine material change more intensely than those of the OV sample, and the curves of the pristine material do not recover to the original position compared with the optimized sample, indicating the local bonding environment of Mn has been changed during the charge-discharge process. The dramatic change of Mn K-edge in the pristine sample after a full charge and discharge cycle indicates the structure of the pristine sample is irreversible.[58] The instability of Mn can mainly be attributed to the production

of Mn^{2+} accompanied by the release of oxygen at high voltage, which also illustrates why the voltage fading is terrible in the pristine material. This result can be supported by the differential electrochemical mass spectra (DEMS) in Fig. 6.[10, 27] The results show the oxygen was detected above 4.5 V for both samples. The oxygen release of OV sample is obviously less than that of the pristine sample. The average amount of oxygen is approximately 0.61 μmol mg^{-1} in the pristine sample. In contrast, the value just is approximately 0.18 μmol mg^{-1} for the OV sample, which means the oxygen vacancies can obviously suppress the evolution of oxygen and enable more lattice oxygen take part in the anion redox chemistry.[10] The reduction of O_2 release is not conducive to the occurrence of side reactions, and this will stabilize the electrolyte and TMs. So, the more stable Mn ion due to less oxygen has been verified by the XANES and DEMS results, which proves there are more excellent cycle performances and weaker voltage decay in the OV sample.[22] The change of the Ni K-edge XANES is more obvious compared with the Mn K-edge in both samples, indicating nickel is involved in the charge compensation in both materials. The spectra of nickel K-edge reversibly move 3.4 eV in the OV sample. However, this change is only approximately 2.9 eV in the pristine material, which means oxygen vacancies and spinel phase are conducive to the electronic conduction and the oxidation of transition metal for the charge compensation, and this is consistent with the following calculation results. Therefore, the electronic conduction of both materials has been carried out with an electrochemical workstation, which shows those of OV and pristine samples are 6.7×10^{-5} S/m and 7.2×10^{-7} S/m, respectively. The increase in electronic conductivity is mainly due to the oxygen

vacancies, which can play as a shallow donor and thus increase the carrier concentration of transition metal oxides.[30, 59, 60] Moreover, Wang et al. have noted that the high MnO_6 octahedral distortion is conducive to the electrochemical performances,[61, 62] and the lower intensity of the white line peak of Mn illustrates a high octahedral distortion of MnO_6, which is likely to enhance the oxygen redox chemistry.[40, 58] Fig. S15† shows the Mn K-edge XANES patterns of before and after 150 cycles. The intensity of the white line peak of OV sample is obviously weaker than that of pristine material meaning a larger MnO_6 octahedral distortion due to oxygen vacancies and spinel phase, which means the OV sample may have a stronger anionic redox activity. This will be further confirmed in the following section.

In addition, soft XAS spectra have been used to further investigate the electronic structure of materials. Fig. S16† shows the transition metal $L_{II,III}$-edge and oxygen K-edge XAS patterns in TEY mode, which are relatively intense and sensitive to the oxidation state and empty TM d orbital because of the electric dipole-allowed 2p → 3d transition.[11, 63] Fig. S16a and d† show there is an obvious change of the Mn peaks in OV sample, which means Mn-ions participated in the charge compensation in the OV sample because of the spinel. It is worth noting that the Mn peaks of both samples changed after the first cycle, which can be ascribed to the irreversible activation of Li_2MnO_3 and the structural rearrangement when charging to above 4.5 V. The Ni L-edge peaks of both samples shift to higher energy state with the voltage increasing as shown in Fig. S16b and e†, indicating Ni is the main charge compensator in the cation.

The O K-edge spectra are shown in Fig. S16c and f†. It is worth noting that the ~529 eV of the pristine material shifts to a lower energy state at 4.8 V, but that of OV material is unchanged, which may be caused by the more oxygen evolution in the pristine sample. As a result, the cation Mn participates in charge compensation due to the spinel phase, and the introduction of oxygen vacancies has suppressed the O_2 release during oxygen redox reaction. As a result, all of these advantages contribute to the improvement of the electrochemical performances. The above analyses have verified the structure stability and cation charge compensation of the OV sample by XAS, however, the high capacity of Li-rich cathode materials also originates from the anionic redox, which has been proved by some groups.[24, 43, 64-67]

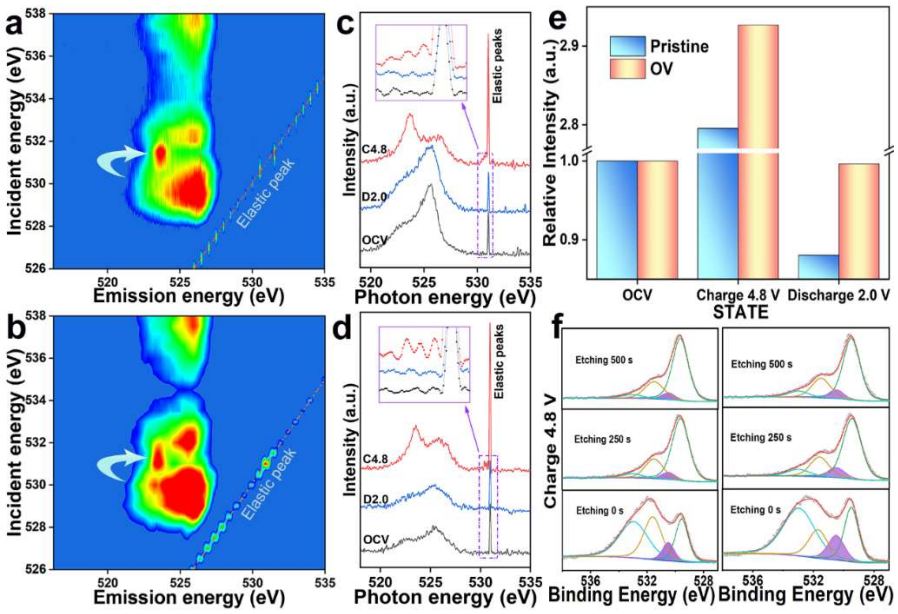

Fig. 7 (a and b) O K-edge RIXS mappings of pristine and OV samples, respectively. O K-edge RIXS spectra of (c) pristine and (d) OV sample with an incident energy of 531 eV at different charge-discharge states (OCV: open circuit voltage; D: discharge; C: Charge). (e) The comparison of the elastic peaks intensity based on the spectra in Fig. c and d. (f) O 1s XPS spectra of pristine (left) and OV (right) samples at 4.8 V, which are performed at different argon ion etching time (0 s, 250 s and 500 s). The purple regions represent the lattice oxygen (O_2^{2-}) at ~530.5 eV. Constant voltage charging for 30 min after constant current charging in both samples.

We used the resonant inelastic X-ray scattering (RIXS) to further verify the activity and reversibility of the oxygen redox in the OV sample due to its higher sensitivity to the state of oxygen compared to the soft XAS spectra. RIXS maps at the oxygen K-edge of pristine and OV samples charged to 4.8 V are displayed in Fig. 7a and b†, respectively. The emission signals around 525 eV are derived from the TM-O hybridization and the general O^{2-} 2p feature.[10] The bright features can be ascribed to the TM 4sp-O 2p and TM 3d-O 2p hybridization located above and below the incident energy of 535 eV, respectively. According to Yang's reports,[10, 51] the obvious RIXS characteristic is a direct evidence of anion redox chemistry as indicated by the arrow located at incident energy and emission energy of 531 and 523.5 eV, respectively. We can find the feature of the OV sample indicated by the arrow having a wider incident energy range compared with that of pristine. This might indicate stronger reactivity of oxygen redox of the OV sample.[68] Moreover, to further analyze the activity and reversibility, the RIXS spectra of both samples have been conducted with 531 eV incident energy under the different charge-discharge stage as shown Fig. 7c and d. We can clearly find that there is a new peak at 523.5 eV when both samples charged to 4.8 V and disappears when discharged to 2.0 V, which is the fingerprint of oxygen redox discussed by the RIXS map. The other interesting change is observed near the elastic peak at 531 eV. There are some weak peaks present for both samples charged to 4.8 V and disappear when discharged to 2.0 V as indicated by the insets shown in Fig. 7c and d. To the best of our knowledge, these peaks are identified for the first time in the Li-rich Mn-based material due to the high-resolution instrument.[69, 70] The peaks of the OV

sample are more obvious as Fig. 7d shows. To understand the implications of the peaks fully would require sophisticated theoretical RIXS knowledge which is still an ongoing effort. However, we think these additional peaks might mean a stronger reactivity of oxygen redox chemistry without change of structure by MnO_6 octahedral distortion rather than large cation rearrangement, which is also consistent with the result of XAS.[12, 62, 71] In addition, the growing intensity of the elastic peak implies the accumulation of more oxygen holes from the oxygen redox chemistry.[12, 71] To have a clear contrast of the reactivity and reversibility of anion redox, histograms are plotted based on the intensity of OCV state as shown in Fig. 7e. We can distinctly find the intensity of the OV sample to be higher than that of pristine state when charge to 4.8 V. This indicates that there is a stronger reactivity of anion redox for the OV sample. The intensity of both samples does not return to the same position as OCV states, which is caused by oxygen loss during cycling.[12, 56, 71] In comparison, the oxygen loss of the pristine sample is much more severe than that of the OV sample indicating a much improved oxygen redox reversibility for the OV sample. In order to investigate the oxygen redox activity in the bulk material, the XPS spectra with different etching time at 4.8 V were conducted as shown in Fig. 7f. Firstly, the obvious change is the peak intensity indexed as electrolyte oxidation species at 533.2 eV after argon etching. Then, the left curves in Fig. 7f shows the almost same peak intensity and shape after argon etching 250 s and 500 s, respectively, and so do the right ones, but both are smaller than that of un-etched surface, indicating the bulk structure has been obtained after etching 250 s. Finally, the oxygen redox activity, O_2^{n-} species, is shown by the purple shadow

area. The proportion of purple area in right image (OV sample) is larger than that of left one (pristine material), meaning there are more peroxy oxygen dimers in the OV sample and more oxygen participate in the charge compensation in the OV sample, which is one reason for the better electrochemical performances than pristine material. Moreover, to illustrate the reversibility of oxygen redox, soft XAS spectra have been collected by FY mode probing the bulk information. Fig. S17a† shows the O K-edge spectra of both samples corresponding to OCV and discharge 2.0 V, respectively. Fig. S17b† shows the integral area between 525 eV and 534 eV, indicating the hole state distribution and the effective charge of oxygen due to the hybridization of O 2p and transition metal 3d.[11] The integral intensity of the OV sample is closer to the initial state when discharge to 2.0 V, suggesting oxygen vacancies and spinel are beneficial to the reversibility of the oxygen redox chemistry, which also interprets the outstanding cyclic ability.

To further investigate the reasons of excellent electrochemical performances of the OV sample, EIS spectra of both samples have been measured before cycling and after 1000 cycles as shown in Fig. S18.† The high-middle frequency plots can be attributed to the solid electrolyte interphase (SEI) resistance and the charge transfer resistance of surface electrodes. As the plots show, the resistances of the OV sample are smaller than those of pristine material whether it is before or after charging, which is well agree with the PITT and electrochemical performances. In addition, the EIS spectrum after cycling at low current density can display indirectly the decomposition

of electrolyte. Fig. S18c† shows the result after 10 cycles at a current density of 25 mA g^{-1}. As the inset shows, the resistance of SEI film is smaller in the OV sample, which means there is less electrolyte was decomposed due to less oxygen reacting with it in the oxygen vacancies sample, which also has been confirmed by the DEMS as shown in Fig. 6. High-resolution transmission electron microscopy (HRTEM) images of the electrode after 250 cycles are more intuitive to interpret this point as shown in Fig. S19.† Fig. S19a and b† show the TEM image of pristine material and OV sample after 1000 cycles, respectively. We can clearly find the SEI film of pristine material is thicker (~6 nm) than that of the OV sample (~2 nm), which can be attributed to the retarded side reaction between the released oxygen and electrolyte due to the existence of oxygen vacancies on the surface. Considering this point, the thermal stability of the OV sample has been also improved by the differential scanning calorimeter (DSC). Fig. S20† shows the DSC collected results of both samples electrode charged to 4.8 V for 30 min. The exothermic peak of pristine is lower, approximately 288.6 ℃ with a higher heat of 338.3 J/g, compared to that of the OV sample at 310.4 ℃ with a much lower heat generation (219.4 J/g). This result of the stable lattice oxygen is in accordance with the DEMS which shows the OV sample has better thermal stability resulting from the existence of oxygen vacancies and spinel phase, which produces less oxygen and fewer side reactions with the electrolyte.

3.3 First-principle Calculations

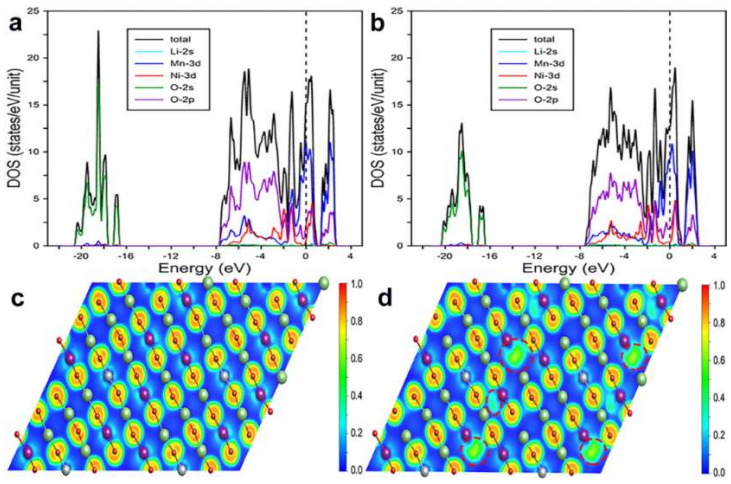

Fig. 8 Electronic structure of both samples. DOS of (a) pristine material (b) OV sample. Maps of ELF for (c) pristine material and (d) OV sample, circles show there are more delocalized electrons around transition metal.

To further confirm and understand the mechanism, the first principle calculations have been conducted based on the density functional theory (DFT). The computational model is built as shown in Fig. S21,† the azury arrows show the sites of oxygen vacancies. Base on this model, the result of density of state (DOS) is computed firstly, and the corresponding results are shown in Fig. 8a and b, respectively. The intensities of DOS are predominated by Mn 3d orbitals near the Fermi level in both samples. Whereas, one thing is worth noting that there is a significant decrease of DOS of O 2p band in the OV sample near the Fermi level in comparison with the pristine sample. This result illustrates the stable lattice oxygen participates in the charge compensation and the oxygen release is suppressed during oxygen redox in the OV sample, which is in good agreement with the electrochemical performances.[40, 72] In order to show the cationic charge compensation more vividly, the isosurface images of electron localization function (ELF) have been carried out in Fig. 8c and d. The red regions represent the lattice electrons, and the blue areas indicate that there are more active

covalent electrons. As observed, the electrons of oxygen and transition metal are more localized as shown in Fig. 8c. As a comparison, there are more delocalized electrons around transition metal when oxygen vacancies are presented as the red dashed circles shown in Fig. 8d. The delocalized electrons might enhance the MnO_6 octahedral distortion due to the asymmetric electronic environment around Mn ion,[58] and all of these indicate both anion oxygen and Mn participate in the charge compensation which is consistent with the results of XAS and electrochemical plots.

The band structure plays an important role in determining the electron conductivity in the cathode materials. Fig. S22† shows both results of the band structure calculation. Fig. S22a and c† show the overall band structure of pristine sample and OV material, respectively. The images of Fig. S22b and d† show the partially enlarged band structure near the Fermi level and the corresponding energy sites have been indexed in the patterns. The computed result shows that the increased overlap of band structure has a stronger metal property in the OV sample compared with the pristine in Fig. S22b and d†, which complies with the experimental result of electron conductivity. The nature of the introduction of oxygen vacancies and spinel phase to modulate the anion and cation redox and achieve the enhanced performances has been well explained by experiment and first-principle computation.

4. Conclusion

Oxygen vacancies and a spinel phase have been successfully introduced to the Li-rich layered material, delivering an enhanced specific capacity, rate capacity and cyclic stability, as well as alleviating the sluggish kinetics and voltage fading. The detailed mechanism of the enhanced electrochemical performances has been studied from both crystal and electronic structure aspects. First, the decreased layer space of TMO_2 is favorable to the structural stability and cyclic stability as revealed by the *in situ* XRD. The expanded Li^+ diffusion tunnel due to the existence of oxygen vacancy and the spinel phase with 3D Li^+ tunnel can improve the Li ion conductivity and rate capacity with a smaller voltage hysteresis. In addition, the increased TM-O bonds and the decreased DOS of O 2p band in the OV sample indicate the reduction of covalency, which alleviates the oxygen release during charge and may benefit the oxygen redox chemistry. The enhancement of MnO_6 octahedral distortion improves the anion and cation redox activity and suppresses the irreversible oxygen generation. We believe this synergetic effect and the detailed mechanism can open a door to some other electrode materials in new energy materials.

Conflicts of interest

There are no conflicts to declare.

Acknowledgements

This work was supported by the National Natural Science Foundation of China (Grant No. 11575192), the International Partnership Program (Grant No.

211211KYSB20170060 and 211211KYSB20180020), the Scientific Instrument Developing Project (Grant No. ZDKYYQ20170001) and “The Hundred Talents Project” of the Chinese Academy of Sciences, Natural Science Foundation of Beijing (Grant No. 2182082), and the University of Chinese Academy of Sciences. The neutron experiments benefit from the SNS user facilities (VULCAN beamline) sponsored by the office of Basic Energy Sciences (BES), the Office of Science of the U.S. DOE. The authors also thank the staffs at the BL08U1-A beamline of SSRF and at beamline 1W1B and 4B7B at BSRF for their support. The allocation of beamtime at RGBL, KMC2 and U41-PEAXIS beamlines, BESSY-II, HZB, Germany, is gratefully acknowledged. We are very grateful to Dr. Yandong Gong, Dr. Yuanyuan Cui and Dr. Ting Yin from Shimadzu China Co., Ltd. for the XPS testing and the discussion.

Supporting Information

Electronic Supplementary Information (ESI) available. See DOI: 10.1039/x0xx00000x

References

1. G. Crabtree, *Science*, 2019, **366**, 422.
2. M. F. Toney, *Nat. Energy*, 2019, **4**, 1014-1015.
3. M. Li, J. Lu, Z. Chen and K. Amine, *Adv. Mater.*, 2018, **30**, 1800561.
4. P. Guan, L. Zhou, Z. Yu, Y. Sun, Y. Liu, F. Wu, Y. Jiang and D. Chu, *J. Energy Chem.*, 2020, **43**, 220-235.
5. J. Lee, D. A. Kitchaev, D.-H. Kwon, C.-W. Lee, J. K. Papp, Y.-S. Liu, Z. Lun, R. J. Clément, T. Shi, B. D. McCloskey, J. Guo, M. Balasubramanian and G. Ceder, *Nature*, 2018, **556**, 185-190.
6. N. H. Vu, J. C. Im, S. Unithrattil and W. B. Im, *J. Mater. Chem. A*, 2018, **6**, 2200-2211.
7. W. H. Kan, B. Deng, Y. Xu, A. K. Shukla, T. Bo, S. Zhang, J. Liu, P. Pianetta, B.-T. Wang, Y. Liu and G. Chen, *Chem*, 2018, **4**, 2108-2123.
8. A. J. Naylor, E. Makkos, J. Maibach, N. Guerrini, A. Sobkowiak, E. Björklund, J. G. Lozano, A. S. Menon, R. Younesi, M. R. Roberts, K. Edström, M. S. Islam and P. G. Bruce, *J. Mater. Chem. A*, 2019, **7**, 25355-25368.
9. M. Li, T. Liu, X. Bi, Z. Chen, K. Amine, C. Zhong and J. Lu, *Chem. Soc. Rev.*, 2020, DOI: 10.1039/C8CS00426A.
10. J. Xu, M. Sun, R. Qiao, S. E. Renfrew, L. Ma, T. Wu, S. Hwang, D. Nordlund, D. Su, K. Amine, J. Lu, B. D. McCloskey, W. Yang and W. Tong, *Nat. Commun.*, 2018, **9**, 947.
11. W. S. Yoon, M. Balasubramanian, K. Y. Chung, X. Q. Yang, J. McBreen, C. P. Grey and D. A. Fischer, *J. Am. Chem. Soc.*, 2005, **127**, 17479-17487.
12. K. Luo, M. R. Roberts, R. Hao, N. Guerrini, D. M. Pickup, Y. S. Liu, K. Edstrom, J. Guo, A. V. Chadwick, L. C. Duda and P. G. Bruce, *Nat. Chem.*, 2016, **8**, 684-691.
13. A. Grimaud, W. T. Hong, Y. Shao-Horn and J. M. Tarascon, *Nat. Mater.*, 2016, **15**, 121-126.
14. A. J. Perez, Q. Jacquet, D. Batuk, A. Iadecola, M. Saubanère, G. Rousse, D. Larcher, H. Vezin, M.-L. Doublet and J.-M. Tarascon, *Nat. Energy*, 2017, **2**, 954-962.
15. X. Li, Y. Qiao, S. Guo, Z. Xu, H. Zhu, X. Zhang, Y. Yuan, P. He, M. Ishida and H. Zhou, *Adv. Mater.*, 2018, **30**, e1705197.
16. M. Sathiya, A. M. Abakumov, D. Foix, G. Rousse, K. Ramesha, M. Saubanere, M. L. Doublet, H. Vezin, C. P. Laisa, A. S. Prakash, D. Gonbeau, G. VanTendeloo and J. M. Tarascon, *Nat. Mater.*, 2015, **14**, 230-238.
17. E. McCalla, A. M. Abakumov, M. Saubanere, D. Foix, E. J. Berg, G. Rousse, M. L. Doublet, D. Gonbeau, P. Novak, G. Van Tendeloo, R. Dominko and J. M. Tarascon, *Science*, 2015, **350**, 1516-1521.
18. T. Nakamura, H. Gao, K. Ohta, Y. Kimura, Y. Tamenori, K. Nitta, T. Ina, M. Oishi and K. Amezawa, *J. Mater. Chem. A*, 2019, **7**, 5009-5019.
19. Y. Liu, Z. Yang, J. Li, B. Niu, K. Yang and F. Kang, *J. Mater. Chem. A*, 2018, **6**, 13883-13893.

20. C. Zhan, T. Wu, J. Lu and K. Amine, *Energy Environ. Sci.*, 2018, **11**, 243-257.
21. M. Ting, M. Burigana, L. Zhang, Y. Z. Finfrock, S. Trabesinger, A. Jonderian and E. McCalla, *Chem. Mater.*, 2020, **32**, 849-857.
22. E. Hu, X. Yu, R. Lin, X. Bi, J. Lu, S. Bak, K.-W. Nam, H. L. Xin, C. Jaye, D. A. Fischer, K. Amine and X.-Q. Yang, *Nat. Energy*, 2018, **3**, 690-698.
23. R. A. House, U. Maitra, M. A. Perez-Osorio, J. G. Lozano, L. Jin, J. W. Somerville, L. C. Duda, A. Nag, A. Walters, K. J. Zhou, M. R. Roberts and P. G. Bruce, *Nature*, 2020, **577**, 502-508.
24. Q. Li, D. Zhou, L. Zhang, D. Ning, Z. Chen, Z. Xu, R. Gao, X. Liu, D. Xie, G. Schumacher and X. Liu, *Adv. Funct. Mater.*, 2019, **29**, 1806706.
25. Y. Wang, L. Tao, Z. Xiao, R. Chen, Z. Jiang and S. Wang, *Adv. Funct. Mater.*, 2018, **28**, 1705356.
26. R. Gao, L. Liu, Z. Hu, P. Zhang, X. Cao, B. Wang and X. Liu, *J. Mater. Chem. A*, 2015, **3**, 17598-17605.
27. B. Qiu, M. Zhang, L. Wu, J. Wang, Y. Xia, D. Qian, H. Liu, S. Hy, Y. Chen, K. An, Y. Zhu, Z. Liu and Y. S. Meng, *Nat. Commun.*, 2016, **7**, 12108.
28. T. Lin, T. U. Schulli, Y. Hu, X. Zhu, Q. Gu, B. Luo, B. Cowie and L. Wang, *Adv. Funct. Mater.*, 2020, DOI: 10.1002/adfm.201909192.
29. Z. Lin, X. Ding, D. Luo, J. Cui, H. Xie and Q. Ren, *Angew. Chem. Int. Ed.*, 2020, DOI: 10.1002/anie.202000628.
30. H. S. Kim, J. B. Cook, H. Lin, J. S. Ko, S. H. Tolbert, V. Ozolins and B. Dunn, *Nat. Mater.*, 2017, **16**, 454-460.
31. K. An, H. D. Skorpenske, A. D. Stoica, D. Ma, X.-L. Wang and E. Cakmak, *Metall. Mater. Trans. A*, 2011, **42**, 95-99.
32. S. Calder, K. An, R. Boehler, C. R. Dela Cruz, M. D. Frontzek, M. Guthrie, B. Haberl, A. Huq, S. A. J. Kimber, J. Liu, J. J. Molaison, J. Neuefeind, K. Page, A. M. dos Santos, K. M. Taddei, C. Tulk and M. G. Tucker, *Rev. Sci. Instrum.*, 2018, **89**, 092701.
33. A. C. Larson and R. B. V. Dreele, *Los Alamos National Laboratory Report LAUR*, 2004, 86-748.
34. G. Kresse and J. Furthmüller, *Comput. Mater. Sci.*, 1996, **6**, 15-50.
35. P. E. Blöchl, *Phys. Rev. B*, 1994, **50**, 17953-17979.
36. J. P. Perdew, K. Burke and M. Ernzerhof, *Phys. Rev. Lett.*, 1996, **77**, 3865-3868.
37. G. Kresse and D. Joubert, *Phys. Rev. B*, 1999, **59**, 1758-1775.
38. D. Marrocchelli, S. R. Bishop, H. L. Tuller and B. Yildiz, *Adv. Funct. Mater.*, 2012, **22**, 1958-1965.
39. L. Li, H. Wang, W. Han, H. Guo, A. Hoser, Y. Chai and X. Liu, *J. Electrochem. Soc.*, 2018, **165**, A3854-A3861.
40. B. Li, H. Yan, J. Ma, P. Yu, D. Xia, W. Huang, W. Chu and Z. Wu, *Adv. Funct. Mater.*, 2014, **24**, 5112-5118.
41. M. Ben Yahia, J. Vergnet, M. Saubanere and M. L. Doublet, *Nat. Mater.*, 2019, **18**, 496-502.
42. J. H. Cheng, C. J. Pan, C. Nithya, R. Thirunakaran, S. Gopukumar, C. H. Chen, J. F. Lee, J. M. Chen, A. Sivashanmugam and B. J. Hwang, *J. Power Sources*,

2014, **252**, 292-297.
43. T. Risthaus, D. Zhou, X. Cao, X. He, B. Qiu, J. Wang, L. Zhang, Z. Liu, E. Paillard, G. Schumacher, M. Winter and J. Li, *J. Power Sources*, 2018, **395**, 16-24.
44. K. Yamamoto, Y. Zhou, N. Yabuuchi, K. Nakanishi, T. Yoshinari, T. Kobayashi, Y. Kobayashi, R. Yamamoto, A. Watanabe, Y. Orikasa, K. Tsuruta, J. Park, H. R. Byon, Y. Tamenori, T. Ohta and Y. Uchimoto, *Chem. Mater.*, 2020, **32**, 139-147.
45. F. Lin, D. Nordlund, Y. Li, M. K. Quan, L. Cheng, T.-C. Weng, Y. Liu, H. L. Xin and M. M. Doeff, *Nat. Energy*, 2016, **1**, 15004.
46. M. Oishi, C. Yogi, I. Watanabe, T. Ohta, Y. Orikasa, Y. Uchimoto and Z. Ogumi, *J. Power Sources*, 2015, **276**, 89-94.
47. E. Beyreuther, S. Grafström, L. M. Eng, C. Thiele and K. Dörr, *Phys. Rev. B*, 2006, **73**, 155425.
48. M. M. Thackeray, J. R. Croy, E. Lee, A. Gutierrez, M. He, J. S. Park, B. T. Yonemoto, B. R. Long, J. D. Blauwkamp, C. S. Johnson, Y. Shin and W. I. F. David, *Sustainable Energy Fuels*, 2018, **2**, 1375-1397.
49. C. M. Julien and M. Massot, *Mater. Sci. Eng. B*, 2003, **97**, 217-230.
50. C. V. Ramana, M. Massot and C. M. Julien, *Surf. Interface Anal.*, 2005, **37**, 412-416.
51. K. Dai, J. Wu, Z. Zhuo, Q. Li, S. Sallis, J. Mao, G. Ai, C. Sun, Z. Li, W. E. Gent, W. C. Chueh, Y.-d. Chuang, R. Zeng, Z.-x. Shen, F. Pan, S. Yan, L. F. J. Piper, Z. Hussain, G. Liu and W. Yang, *Joule*, 2019, **3**, 518-541.
52. Q. Li, Y. Qiao, S. Guo, K. Jiang, Q. Li, J. Wu and H. Zhou, *Joule*, 2018, **2**, 1134-1145.
53. Y. Liu, D. Ning, L. Zheng, Q. Zhang, L. Gu, R. Gao, J. Zhang, A. Franz, G. Schumacher and X. Liu, *J. Power Sources*, 2018, **375**, 1-10.
54. D. Ye, G. Zeng, K. Nogita, K. Ozawa, M. Hankel, D. J. Searles and L. Wang, *Adv. Funct. Mater.*, 2015, **25**, 7488-7496.
55. H. Wang, R. Gao, Z. Li, L. Sun, Z. Hu and X. Liu, *Inorg. Chem.*, 2018, **57**, 5249-5257.
56. H. Koga, L. Croguennec, M. Ménétrier, P. Mannessiez, F. Weill, C. Delmas and S. Belin, *J. Phys. Chem. C*, 2014, **118**, 5700-5709.
57. E. M. Erickson, H. Sclar, F. Schipper, J. Liu, R. Tian, C. Ghanty, L. Burstein, N. Leifer, J. Grinblat, M. Talianker, J.-Y. Shin, J. K. Lampert, B. Markovsky, A. I. Frenkel and D. Aurbach, *Adv. Energy Mater.*, 2017, **7**, 1700708.
58. Z. Lun, B. Ouyang, D. A. Kitchaev, R. J. Clément, J. K. Papp, M. Balasubramanian, Y. Tian, T. Lei, T. Shi, B. D. McCloskey, J. Lee and G. Ceder, *Adv. Energy Mater.*, 2019, **9**, 1802959.
59. G. Wang, Y. Ling and Y. Li, *Nanoscale*, 2012, **4**, 6682-6691.
60. S. K. Deb, *Phys. Rev. B*, 1977, **16**, 1020-1024.
61. S. Li, X. Meng, Q. Yi, J. A. Alonso, M. T. Fernández-Díaz, C. Sun and Z. L. Wang, *Nano Energy*, 2018, **52**, 510-516.
62. J. Hong, W. E. Gent, P. Xiao, K. Lim, D. H. Seo, J. Wu, P. M. Csernica, C. J.

Takacs, D. Nordlund, C. J. Sun, K. H. Stone, D. Passarello, W. Yang, D. Prendergast, G. Ceder, M. F. Toney and W. C. Chueh, *Nat. Mater.*, 2019, **18**, 256-265.
63. S. Hy, W.-N. Su, J.-M. Chen and B.-J. Hwang, *J. Phys. Chem. C*, 2012, **116**, 25242-25247.
64. M. Sathiya, G. Rousse, K. Ramesha, C. P. Laisa, H. Vezin, M. T. Sougrati, M. L. Doublet, D. Foix, D. Gonbeau, W. Walker, A. S. Prakash, M. Ben Hassine, L. Dupont and J. M. Tarascon, *Nat. Mater.*, 2013, **12**, 827-835.
65. B. Li and D. Xia, *Adv. Mater.*, 2017, **29**, 1701054.
66. G. Assat and J.-M. Tarascon, *Nat. Energy*, 2018, **3**, 373-386.
67. X. Zheng, P. Li, H. Zhu, K. Rui, G. Zhao, J. Shu, X. Xu, W. Sun and S. X. Dou, *Energy Storage Mater.*, 2018, **15**, 257-265.
68. S. Li, S.-J. Lee, X. Wang, W. Yang, H. Huang, D. S. Swetz, W. B. Doriese, G. C. O'Neil, J. N. Ullom, C. J. Titus, K. D. Irwin, H.-K. Lee, D. Nordlund, P. Pianetta, C. Yu, J. Qiu, X. Yu, X.-Q. Yang, E. Hu, J.-S. Lee and Y. Liu, *J. Am. Chem. Soc.*, 2019, **141**, 12079-12086.
69. K. Lieutenant, T. Hofmann, C. Schulz, M. V. Yablonskikh, K. Habicht and E. F. Aziz, *J. Electron Spectrosc. Relat. Phenom.*, 2016, **210**, 54-65.
70. C. Schulz, K. Lieutenant, J. Xiao, T. Hofmann, D. Wong and K. Habicht, *J. Synchrotron Radiat.*, 2020, **27**, 238-249.
71. K. Luo, M. R. Roberts, N. Guerrini, N. Tapia-Ruiz, R. Hao, F. Massel, D. M. Pickup, S. Ramos, Y. S. Liu, J. Guo, A. V. Chadwick, L. C. Duda and P. G. Bruce, *J. Am. Chem. Soc.*, 2016, **138**, 11211-11218.
72. J. Ma, H. Yan, B. Li, Z. Xia, W. Huang, L. An and D. Xia, *J. Phys. Chem. C*, 2016, **120**, 13421-13426.

TOC

The activity and reversibility of both anionic and cationic redox in cobalt-free Li-rich Mn based cathode have been improved by integrating oxygen vacancy and spinel phase, and the underlying modulation mechanism has been unraveled.